Guan et al. *NPG Asia Materials* (2023)15:60
https://doi.org/10.1038/s41427-023-00508-6

NPG Asia Materials

ARTICLE Open Access

Izod impact resistance of 3D printed discontinuous fibrous composites with Bouligand structure

Lizhi Guan[1], Weixiang Peng[1], Rachel Ng Jing Wen[2], Jingbo Fan[2] and Hortense Le Ferrand[1,2,3]

Abstract

The Bouligand structure found in the dactyl club of mantis shrimps is known for its impact resistance. However, Bouligand-inspired reinforced composites with 3D shapes and impact resistance characteristics have not yet been demonstrated. Herein, direct ink writing was used to 3D print composites reinforced with glass microfibers assembled into Bouligand structures with controllable pitch angles. The energy absorption levels of the Bouligand composites under impact were found to surpass those of composites with unidirectional microfiber alignment. Additionally, the Bouligand composites with a pitch angle of 40° exhibited a maximum energy absorption of 2.4 kJ/m^2, which was 140% higher than that of the unidirectional composites. Furthermore, the characterization of the topography of the fractured surface, supplemented with numerical simulations, revealed a combination of crack twisting and crack bridging mechanisms. Flexural tests conducted on the composites with a pitch angle of 40° revealed that these composites had the strongest properties, including a flexural strength of 36.9 MPa, a stiffness of 2.26 GPa, and energy absorption of 8 kJ/m^2. These findings are promising for the microstructural design of engineered composites using direct ink writing for applications in aerospace, transportation, and defense.

Introduction

The microstructural design of reinforced composites significantly influences their mechanical properties, particularly their resistance to catastrophic failure. Researchers have been inspired by the microstructures found in biological materials to create artificial composites with good strength and toughness[1]. One remarkable biological composite is the dactyl club of mantis shrimps, which can withstand impact and cavitation forces of 1501 and 504 N, respectively[2]. Scholars have previously reported that the periodic region in the dactyl club contributes most to its impact resistance due to the helicoidal arrangement of mineral nanorods in a Bouligand structure[3]. In this structure, layers of aligned mineral nanorods are stacked with a small angle turn between each adjacent layer[3]. The pitch angle provides the Bouligand structure shear wave filtering effect and enhances its energy absorption upon fracture[4]. Synthetic composites with Bouligand structures have shown promising results. For example, Bouligand cement composites reinforced with discontinuous steel fibers of ~12 mm length have shown toughness under drop-weight impact because of mixed modes of fracture with crack deflection, twisting, branching, bridging, and microcracking[5]. Bouligand composites reinforced with continuous glass fibers tested under Charpy impact exhibit an increase in energy absorption attributed to crack twisting[6], while under quasistatic fracture, they exhibit a combination of crack twisting and crack bridging[7]. However, to the best of the authors' knowledge, the impact resistance mechanisms of Bouligand composites have not yet been investigated in notched samples. Additionally, microfiber-reinforced composites with Bouligand structure, 3D morphology, and impact resistance characteristics have yet to be demonstrated.

Correspondence: Hortense Le Ferrand (hortense@ntu.edu.sg)
[1]School of Mechanical and Aerospace Engineering, Nanyang Technological University, 50 Nanyang Avenue, Singapore 639798, Singapore
[2]School of Materials Science and Engineering, Nanyang Technological University of Singapore, 50 Nanyang Avenue, Singapore 639798, Singapore
Full list of author information is available at the end of the article
These authors contributed equally: Lizhi Guan, Weixiang Peng

To create Bouligand composites, one strategy consists of manually laying up long fiber-reinforced polymer laminates with controlled angles between each layer[8–10]. However, the use of continuous long fibers poses drastic constraints on the shapes. In contrast, the use of short fibers allows the creation of liquid inks or pastes that can be used in additive manufacturing processes. For instance, Bouligand composites have been produced by brush-induced assembly of short micro/nanofibers on a heated substrate[11]. In other works, adjusting the pH, aspect ratio, and concentration values of chitin whiskers in a solution can trigger their self-assembly into a Bouligand structure[12]. However, these strategies still face limitations in terms of scalability, control of the Bouligand pitch angle, freedom to achieve complex 3D shapes and overall efficiency. Having a fabrication method that can tailor the structural parameters, such as the pitch angle, can allow the rational design and optimization of the Bouligand structure for high impact resistance in fiber-reinforced composites.

To enable such rational structural design, an efficient fabrication approach is 3D printing. To align microfibers at any desired angle, 3D printing has been combined with external fields[13]. For example, stereolithographic 3D printing has been combined with electric fields to align carbon nanotubes (CNTs) within each deposited layer[14]. However, stereolithography requires a liquid resin that is cured using ultraviolet (UV), which limits the loading and mechanical properties of CNTs. In contrast, extrusion-based 3D printing techniques, such as fused deposition modeling (FDM) and direct ink writing (DIW), do not have these limitations. In FDM, thermoplastic filaments are melted, extruded, and deposited on a cool substrate, whereas DIW involves pushing viscous inks with shear-thinning and thixotropic properties through a nozzle on a substrate. Because of the extrusion at the nozzle in both methods, shear can lead to alignment along the printing direction of the microfibers distributed in the filaments or ink[15]. To form Bouligand structures, it is sufficient to control the direction in which the nozzle is moving in each layer to set the orientations of microfibers present in the extruded material[14]. Using FDM, Bouligand structures have been manufactured, showing improvements in their specific impact energies[6]. However, delamination of the composite occurs during failure, likely due to the inevitable voids between the extruded lines resulting in weak interfaces. In addition, FDM has constraints on the achievable fiber concentration and thus on the achievable mechanical properties. These issues are serious for future practical and commercial applications. In contrast, DIW has been shown to be capable of 3D printing a wide variety of compositions, including viscous inks with high concentrations in reinforcing particles[16]. Using DIW to 3D print Bouligand structures can potentially overcome the limitations of FDM and achieve improved mechanical properties while enabling fine control over the microstructure to test and understand energy-dissipating mechanisms during fracture.

In this work, epoxy composites reinforced with glass microfibers assembled into Bouligand structures with controllable pitch angles are 3D printed using DIW, and their impact resistance and flexural properties are tested. Numerical simulations are conducted to support the experimental results to study the fracture mechanisms. First, the rheological properties of viscous inks containing glass microfibers are optimized to yield a printable ink using DIW that aligns glass microfibers along the printing direction. Subsequently, Izod impact tests are conducted on notched 3D printed composites to compare the energy absorption levels of unidirectional and Bouligand structures. The fractured specimens are inspected using scanning electron microscopy (SEM), laser microscopy, and micro-computed tomography (micro-CT), which allow the characterization of the surface morphology, porosity, and cracking mechanisms. The flexural properties of the composites are tested to compare the dynamic with the quasistatic fracture behaviors. The findings from this study provide insights into 3D printed, lightweight, and impact-resistant reinforced composites for potential applications in the aerospace, automotive, and defense industries, among others.

Materials and methods

Materials

Carbon black was obtained from PRINTEX® XE 2-B, and multiwalled CNTs (MWCNTs) were obtained from Graphistrength® Arkena Innovative Chemistry. E-glass fibers (milled glass microfibers) were sourced from Japan's Nippon Electric Glass Co. The lengths and diameters of the microfibers ranged from 20–300 μm and 7–14 μm, respectively, with average values of 50 μm and 10 μm (see Supplementary Information (SI) Fig. S1). Commercial epoxy resin and epoxy hardener (Casting Resin MS1000) were purchased from WEICON Southeast Asia Pte Ltd.

Methods

Ink preparation

MWCNTs (0.15 g) and carbon black (0.03 g) were dispersed into 7.98 g of epoxy resin using a Thinky Mixer (THINKY ARE-250, Japan) for 5 min at 2000 rpm. Subsequently, 5.25 g of glass microfibers was added to the above mixture and mixed for 5 min at 1000 rpm using an overhead mixer (Base Hei-TORQUE VALUE 400, Heidoph Instruments GmbH & Co. KG, Germany). Afterward, 1.59 g of epoxy hardener was introduced and mixed using the same overhead mixer for 5 min at 500 rpm at a cold temperature in an ice bath. The slow speed of the mixing and the use of the ice bath reduced the heat generated from the mixing and

slowed the epoxy reaction and consolidation of the mixture, which was the ink utilized for DIW.

DIW of the Bouligand composites

The 3D printing assembly (3D Potter Micro 8, 3D Potter Inc. USA) consisted of a vertical nozzle with a mechanical piston to extrude the ink through the nozzle. The 3D models were created using computer-aided design software (Rhinoceros 7). IdeaMaker was used to slice the designs into layers for printing. Unidirectional microfibers orientation at angles of $\alpha = 0°$, 45°, and 90° within all the layers and Bouligand structures with various pitch angles of $\gamma = 10°$, 20°, 40°, 60°, and 90° were designed. To realize these goals, the 3D printer first deposited a layer with aligned glass fibers and then deposited another layer with a printing direction twisted at the pitch angle to obtain Bouligand structures in the composites.

The following printing parameters were used: a diameter nozzle of 0.8 mm, printing speed of 8 mm/s, layer thickness of 0.4 mm, and flow rate of 50%. At least six specimens of each design were printed for each test. The length, width, and depth values of the printed specimens were 64 mm, 6 mm, and 12.8 mm, respectively. For these dimensions, 32 layers were deposited on top of each other. Since the total number of layers was fixed and the pitch angle was varied, the period of the helicoidal assembly increased as the pitch angle increased:

$$\text{period} = \frac{32 * \gamma}{180}. \quad (1)$$

Therefore, the periods of the Bouligand structures with $\gamma = 10°$, 20°, 40°, 60°, and 90° were 1.8, 3.5, 7.1, 10.7, and 16, respectively (see SI Fig. S2 for the schematics of the 3D printed structures).

Impact tests and characterization

Izod impact tests were conducted using the Tinius Olsen impact machine (Willow Grove, PA, U.S.A.) following the ASTM standard D256. A V-notch of 2 mm depth was cut using a sample notch tool (DS-93). The dimensions of the impacted samples were as follows: 64 mm (length, l), 12 mm (width, b_N) and 4 mm (thickness, h). The applied pendular energy was 3.3669 J. The impact speed rate was 3.5 m/s (see SI Fig. S3 for a schematic of the set-up). The impact energy absorption E_a expressed in kJ/m^2 was calculated using the following equation:

$$E_a = \frac{E_c}{h \cdot b} \times 10^3 \quad (2)$$

where E_c is the corrected energy absorbed by the specimen (in joules); h is the thickness of the specimen (in mm); and b is the remaining width (in mm) of the specimen after testing. The specimens were polished using SiC papers before impact testing.

The methods used for the other characterizations are described in the SI.

Finite element modeling

Finite element (FE) analysis was conducted using Abaqus 2020 (see Supplementary Text in SI for more details). The model was composed of glass microfibers (length: 25 μm, diameter: 5 μm, and aspect ratio: 5) assembled into Bouligand structures with the desired pitch angle γ and surrounded by a matrix meshed with solid elements C_3D_4. The fiber-matrix interface was simulated with cohesive elements. The simulated samples had representative geometric dimensions of 325 μm × 810 μm × 214 μm (length × width × depth). The volume content of the microfibers (20 vol%) used in the numerical simulation was the same as that in the experiment. All the material properties used in the simulations are listed in Tables S1 and S2. The tensile stress–strain response of the pure matrix without glass microfibers was measured experimentally (see SI Fig. S4).

Results

DIW of the Bouligand composites

To enable the design and fabrication of the Bouligand composites using 3D printing, the concentration of glass microfibers in the epoxy resin had to be adjusted to ensure printability (Fig. 1). The ink was required to have a high viscosity and a high yield stress to allow extrusion and shape retention, respectively, and the possibility to print multiple layers without the collapse of the structure[17]. Glass microfibers (50 μm in width and 10 μm in diameter on average) were used for the reinforcements. These glass microfibers were similar in chemistry to those used in continuous long fiber composites, but the short size was necessary to permit the creation of complex shapes with good resolution *via* 3D printing. The dimensions of the microfibers were important since they bore a significant percentage of the applied load[18]. Here, the aspect ratio of the microfibers ranged from 2 to 30, with an average value of 5 (Fig. 1a). To meet the rheological requirements for DIW, carbon black and MWCNTs were introduced in the ink by following a previous procedure[19]. These additional nanomaterials could enhance the final mechanical performance, although this enhancement was not the focus of this study. The ink was optimized to efficiently enable the homogeneous dispersion of the constituents and the removal of the air bubbles. The finalized optimized ink contained 35 wt% glass microfibers and had a viscosity at rest of 1000 Pa·s and a

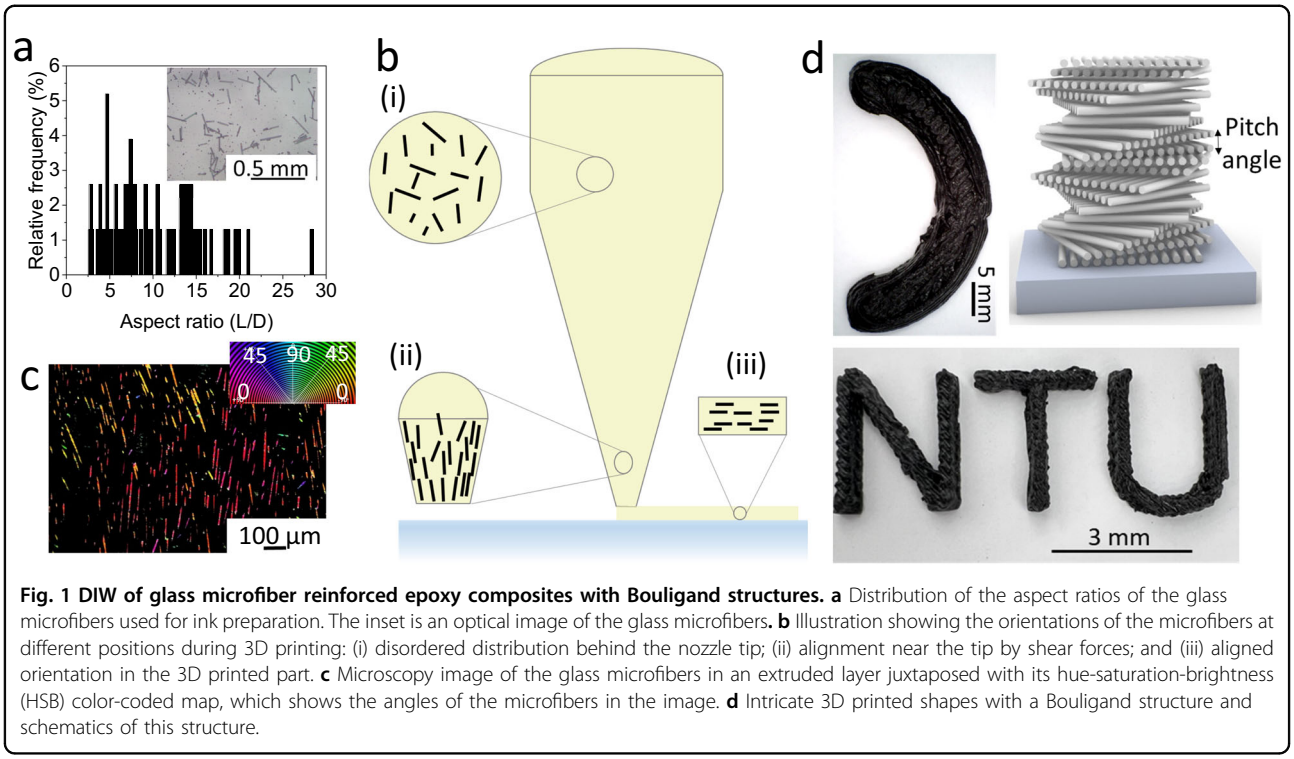

Fig. 1 DIW of glass microfiber reinforced epoxy composites with Bouligand structures. a Distribution of the aspect ratios of the glass microfibers used for ink preparation. The inset is an optical image of the glass microfibers**. b** Illustration showing the orientations of the microfibers at different positions during 3D printing: (i) disordered distribution behind the nozzle tip; (ii) alignment near the tip by shear forces; and (iii) aligned orientation in the 3D printed part. **c** Microscopy image of the glass microfibers in an extruded layer juxtaposed with its hue-saturation-brightness (HSB) color-coded map, which shows the angles of the microfibers in the image. **d** Intricate 3D printed shapes with a Bouligand structure and schematics of this structure.

yield stress of 500 Pa (see SI Fig. S5 for the rheological data), which allowed 3D printing. After the ink was mixed, it was immediately transferred into the 3D printing syringe before the epoxy matrix was cured (see SI Fig. S5 for the viscosity of the resin as a function of time). In practice, the curing reaction could be slowed by using an epoxy matrix that crosslinked upon application of an external trigger, such as a low temperature. The aim of this study was to understand the mechanisms and the extent of impact resistance due to the Bouligand structure; thus, the resin and its curing time were chosen arbitrarily. During DIW, the glass microfibers transitioned from a random orientation behind the nozzle tip (Fig. 1b (i)) to an aligned orientation along the walls of the nozzle at the tip (Fig. 1b (ii))[15]. After extrusion and deposition, the microfibers maintained their orientation, which was further fixed by the increase in viscosity due to the curing of the resin (Fig. 1b (iii)). This orientation of the microfibers after 3D printing was verified by optical microscopy (Figs. 1c and SI Fig. S6)[20]. The precise alignment of the glass microfibers could therefore be combined with complex 3D shapes (Fig. 1d). The 3D microstructures in printed parts of complex shapes could be resolved using micro-CT (see SI Video S1 for the micro-CT scan of a Bouligand structure with a pitch angle of 90°). After curing, the printed reinforced composites retained their shape and microstructure and had a low density of 1.4 g/mL.

Impact energy absorption

The control of the microstructure during 3D printing was convenient for studying the effects of microstructural design on impact resistance[21]. First, we designed and fabricated composites with unidirectional microfiber orientations (Fig. 2). To observe the effect of fiber orientation on crack propagation, the composites were purposely printed and tested at various microfiber angles α with respect to the impact direction (e.g., $\alpha = 0°$ represented microfibers parallel to the impact direction). Composites with microfibers oriented at $\alpha = 0°$, 45°, and 90° were successfully 3D printed, notched, and submitted to the Izod impact test (Fig. 2a). As shown in Fig. 2b, the energy absorption of all unidirectional composites was higher than that of the control composite without glass microfibers. Increasing α increased the impact energy absorption of the composites from 0.514 kJ/m^2 for $\alpha = 0°$ to 1.1 kJ/m^2 for $\alpha = 90°$. To explore the toughening mechanisms, the morphology of the fractured surface was captured for each microstructure (Fig. 2c–f). The control composites presented a straight crack along the notched direction. The addition of microfibers with an $\alpha = 0°$ orientation showed a very straight crack along the notched direction, which was parallel to the microfibers. From the electron micrographs in Fig. 2d, crack slippage along the microfibers resulted in river-like structures with hackles and ribbons at the fractured surface, which

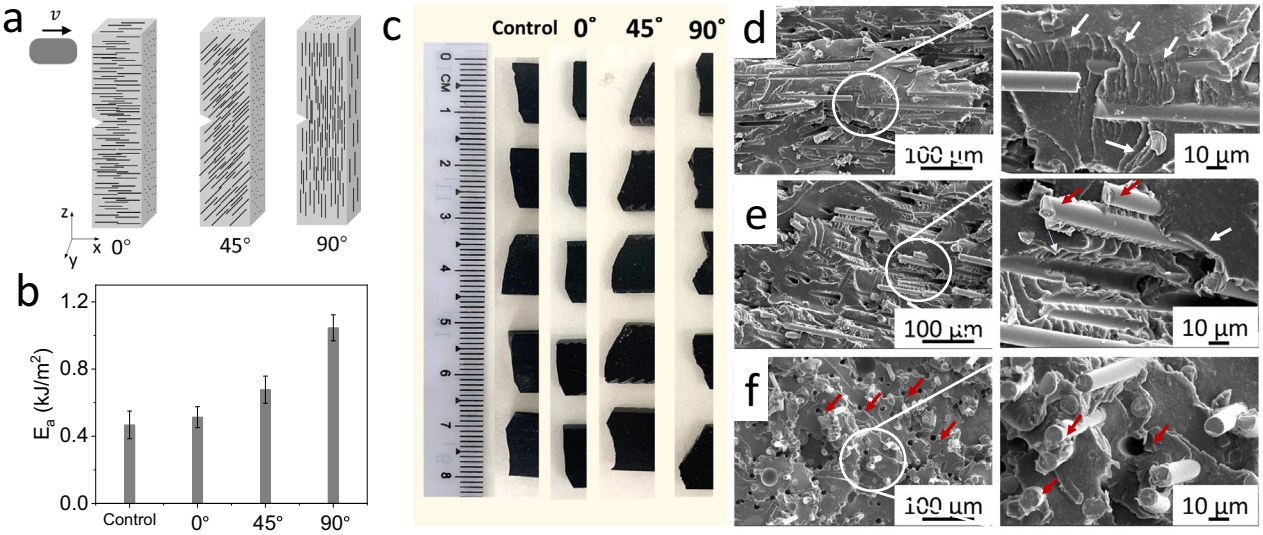

Fig. 2 Impact tests on composites with unidirectional microfiber orientations at 0°, 45°, and 90°. a Illustrations showing the microstructures of composites with microfibers oriented at angles of $\alpha = 0$, 45, and 90° prepared for the Izod impact test. **b** Energy absorption E_a for control composites (no microfibers) and reinforced composites with increasing angle α. **c** Pictures of the fractured composites after the impact tests. Electron micrographs of the composites with unidirectional orientation at (**d**) $\alpha = 0°$, (**e**) $\alpha = 45°$, and (**f**) $\alpha = 90°$. White arrows indicate river-like structures with hackles and ribbons. Red arrows indicate the pull-out and breakage of the glass microfibers.

contributed to increasing the energy absorption relative to the control composites. These types of white marks are typical of ductile deformation of the matrix in the presence of reinforcements[22]. Because there was no increase in crack tortuosity between the control composites and the composites with $\alpha = 0°$, the difference in energy absorption was negligible. However, increasing the orientation angle to $\alpha = 45°$ deviated the crack from the notch direction following the microfiber orientations, extending the crack length and increasing the energy absorption. Additionally, it could be observed that some glass microfibers were removed from the matrix (red arrows in Fig. 2e). This phenomenon, along with crack slippage, contributed to these composites exhibiting higher energy absorption levels than the composites with $\alpha = 0°$. Upon further increasing the orientation angle to $\alpha = 90°$, the fractured surface morphology appeared increasingly rough. Electron micrographs showed that most microfibers were pulled out and broken during impact, indicating the presence of a crack bridging mechanism (Fig. 2f). Crack deflection led to increased tortuosity, and the presence of microfibers perpendicular to the notch and crack propagation directions increased the energy dissipation. Overall, these series of experiments provided insights into the modes of fracture propagation in our microfiber-reinforced composites. At angles below 45°, the crack tended to propagate along the microfibers with a minor increase in the total energy absorption. Increasing the orientation angle to 90° resulted in a relatively great degree of crack deflection and energy absorption with increasing microfiber fracture. From $\alpha = 0°$ to 90°, a transition between two fracture mechanisms was observed with slippage at low angles and pull-out and broken fiber at relatively high angles. Furthermore, there was some correlation between an increased impact energy absorption and an increased surface roughness. How the surface morphology and topography reflected the failure behavior has been reported in several studies[23–25]. Therefore, tailoring the microstructure to significantly enhance the surface roughness could be expected to further amplify the energy absorption during fracture. We verified this hypothesis next in composites with 3D printed Bouligand structures ($\alpha = 90°$).

To demonstrate that the Bouligand microstructure could create rough fractured surfaces and increase energy absorption, we 3D printed composites with pitch angles of $\gamma = 0°$, 10°, 20°, 40°, 60° and 90° (Fig. 3). By conducting the same impact tests as for unidirectional composites, increased energy absorption was recorded for all pitch angles (Fig. 3a). The minimum energy absorption level of the Bouligand composites was obtained at $\gamma = 10°$, with a value of 1.5 kJ/m^2. By increasing the pitch angle to $\gamma = 40°$, a maximum energy absorption of 2.48 kJ/m^2 was obtained. Beyond $\gamma = 40°$, the composites exhibited relatively low impact resistance to 1.6 kJ/m^2 at $\gamma = 90°$. The excellent energy absorption levels of the Bouligand composites relative to the unidirectional composites were attributed to the Bouligand structures, revealing an optimum pitch angle at which the energy absorption is at a

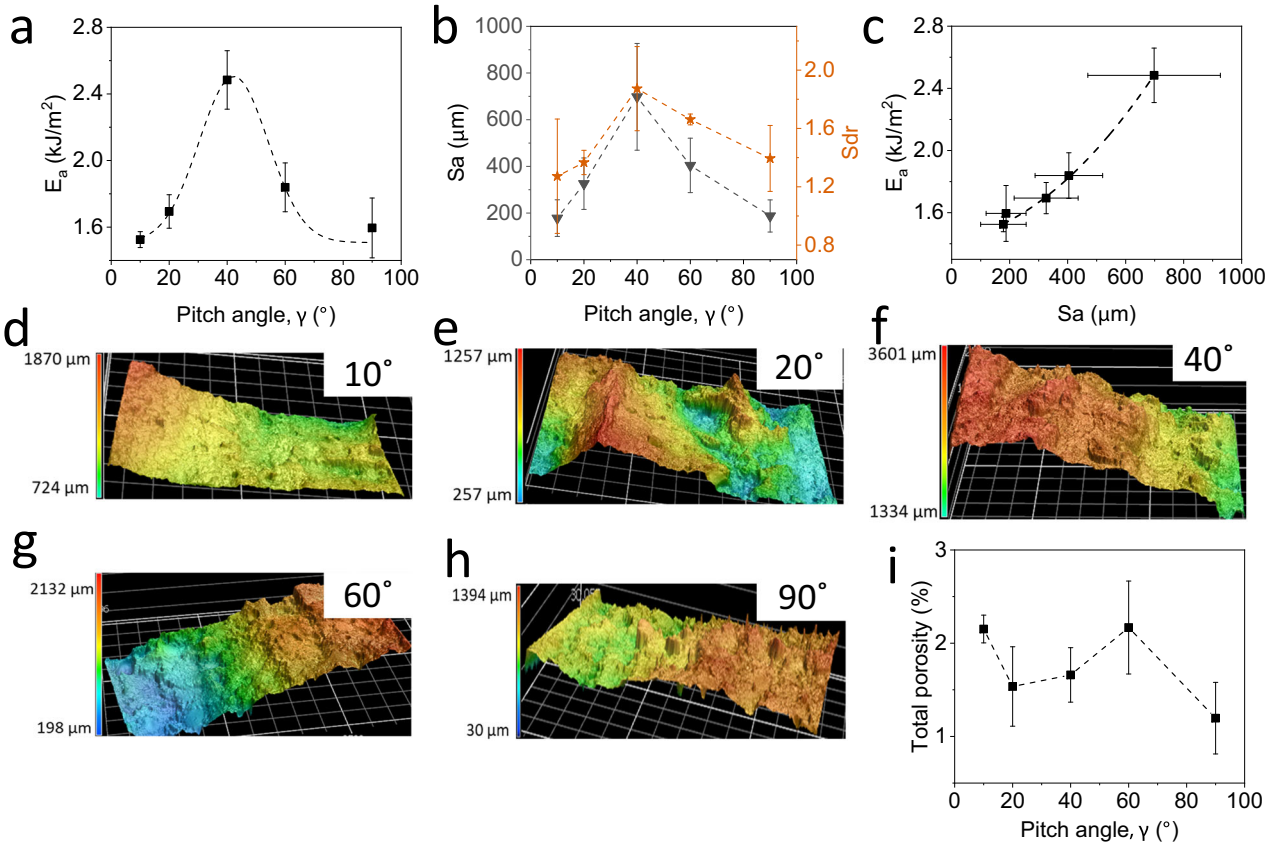

Fig. 3 Impact performance of the Bouligand composites at various pitch angles. a Impact energy absorption and (**b**) the fractured surface roughness values of the composites with the Bouligand structure as a function of the pitch angle γ. Dotted lines are guides to the eye. **c** Energy absorption as a function of the surface roughness. The dotted line is an exponential fit with the coefficient of correlation $R^2 = 0.99$. (**d**–**h**) Topographies of the fractured surface of the Bouligand composites for each pitch angle. The images show that fracture propagates from left to right. **i** Total porosities of the composites as a function of the pitch angle.

maximum value. The angle 40° seemed to give the best properties for our composites. This phenomenon was different from Bouligand structures made from other materials, which showed a maximum toughness at a highly reduced pitch angle of approximately 9.47°[6]. This result likely occurred due to the differences in chemical composition and microfiber size. Indeed, it has been reported that the aspect ratio of the microfiber drastically modified the responses of composites[7]. To better understand the performance of our Bouligand composites and to verify the importance of the pitch angle, we carefully analyzed the fractured surfaces. Precisely, we measured the surface topographies of the fractured surfaces and quantified the surface arithmetical mean roughness Sa values and the developed interfacial area ratio Sdr values. As depicted in Fig. 3b, increasing the pitch angle increased Sa and Sdr from 180 μm and 1.3, respectively, at $\gamma = 10°$ to the maximum values of 600 μm and 1.9, respectively, at $\gamma = 40°$. At high pitch angles, Sa and Sdr decreased again to 190 μm and 1.4, respectively, at $\gamma = 90°$. Interestingly, the impact energy absorption E_a was found to vary exponentially with Sa with a coefficient of correlation $R^2 = 0.99$ (Fig. 3c). Such an exponential correlation between roughness and energy absorption was analogous to the exponential correlation between roughness and flexural toughness reported elsewhere[23]. Furthermore, the morphologies of the entire fractured surfaces were obtained through reconstructed 3D views (Fig. 3d–h). In the Bouligand composites with $\gamma = 10°$ (Fig. 3d), the fractured surface was relatively smooth, and the crack slipped along the microfibers (see SI Fig. S7 for electron micrographs of the fractured surfaces), which indicated crack twisting as the dominant fracture mechanism. The fracture surface of the composites with $\gamma = 20°$ displayed two mountain-like features that were the result of crack deflections along the microfiber orientations. The peaks of the mountains likely correspond to the areas where the microfibers were at 90°. Within the scanned area, there were four structural periods, and it was expected that the microfibers reached orientations of 90° four times, but

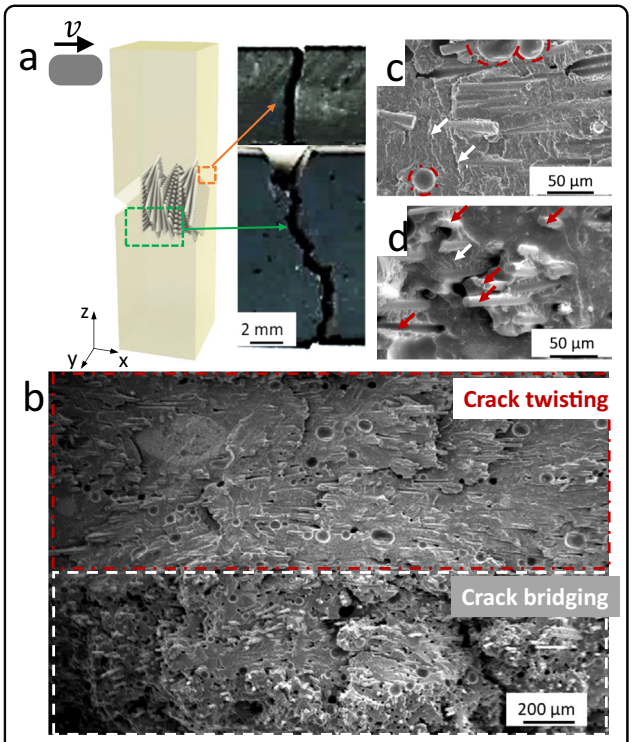

Fig. 4 Fractured morphologies of the Bouligand composites with a pitch angle of 40°. a Illustration and images of the fractured specimen in the XZ plane (green color) and in the YZ plane (orange color). **b** Electron micrograph of the fractured surface showing crack twisting and crack bridging regions and zoomed-in micrographs in (**c**) and (**d**), respectively. The red circles indicate microvoids, the red arrows indicate broken microfibers, and the white arrows indicate cracks in the epoxy matrix.

only two mountain-like features were observed. One probable reason for this discrepancy was that the fracture of composites was a complex process that could not be predicted with 100% accuracy, particularly in our composites where defects such as bubbles and misalignments were present. Nevertheless, the trends observed experimentally correlated well with the microstructures. Apart from the two mountain-like regions, the rest of the fractured surface was relatively smooth (see SI Fig. S7 for electron micrographs of the fractured surface). As the pitch angle increased further to $\gamma = 40°$, the surface roughness of the fracture surface increased with further fracture of the microfibers and with large crack deflection events. Beyond $\gamma = 40°$, the topographies of the fractured surfaces appeared relatively smooth with continuous crack paths (Fig. 3g, h). Overall, the cracking mechanisms in the Bouligand composites included crack twisting and crack bridging. When both mechanisms occurred, the fracture surface area was amplified, resulting in increased energy absorption. The transition from the predominantly crack twisting mode at small pitch angles to the predominantly crack bridging mode at high pitch angles has been reported in other works, but at relatively small pitch angles, as discussed previously[7]. Our results demonstrated that by carefully tuning the pitch angle by 3D printing, it was possible to tailor the fractured surface roughness to achieve maximum energy absorption. This enhancement in the impact resistance came despite the presence of certain defects, such as gaps, bubbles, and misalignment, that could not be avoided. We indeed measured a small amount of porosity in our composites (Fig. 3i), which could contribute positively to the energy absorption[6]. Overall, the impact resistance achieved in our 3D printed Bouligand composites was quite remarkable.

The Bouligand composites with a pitch angle of 40° exhibited the highest energy absorption during impact. A closer look at the topography of the fracture surface further confirmed the fracture mechanisms discussed above (Fig. 4). High crack tortuosity along the impact direction (in the XZ plane) likely resulted from a combination of crack twisting and crack bridging (green color in Fig. 4a). The straight crack path in the YZ plane at the back of the composite (orange color) suggested that the crack propagated along the direction of the microfibers within each aligned layer. From the electron micrographs in Fig. 4b, two regions could be highlighted. The top region framed by the red dotted lines presented a smooth fracture surface topography because the crack propagated along the microfiber orientation. This phenomenon was confirmed by the image at a high resolution shown in Fig. 4c. In contrast, the bottom region framed by the white dotted lines showed a relatively rough surface topography, and many glass microfibres were pulled out and broken, which was confirmed at high resolutions (Fig. 4d). Therefore, the combined crack twisting and bridging mechanisms contributed to the high impact energy absorption levels in Bouligand composites with a pitch angle of 40°.

Numerical simulation analysis

To confirm the experimental results, numerical simulations were conducted using the finite element method (Figs. 5 and SI Figs. S8–S10 and supplementary text for details about the simulations)[26]. The mechanical properties of the matrix were obtained experimentally (see SI Table S1). The Johnson–Cook constitutive model parameters of the matrix were obtained by fitting the experimental stress–strain curves. The simulation model used the optimal alignment of glass microfibers with a length of 25 μm, diameter of 5 μm, and aspect ratio of 5 in composites without porosity. While other input parameters, such as the cohesive behaviors for interface properties and the continuum damage model for the epoxy matrix, were sourced from the literature (see SI supplementary text and Figs. S8–10)[26], these parameters were proven to be successful in epoxy and microfiber systems in FEM simulations. Given that the simulation model relied on the ideal

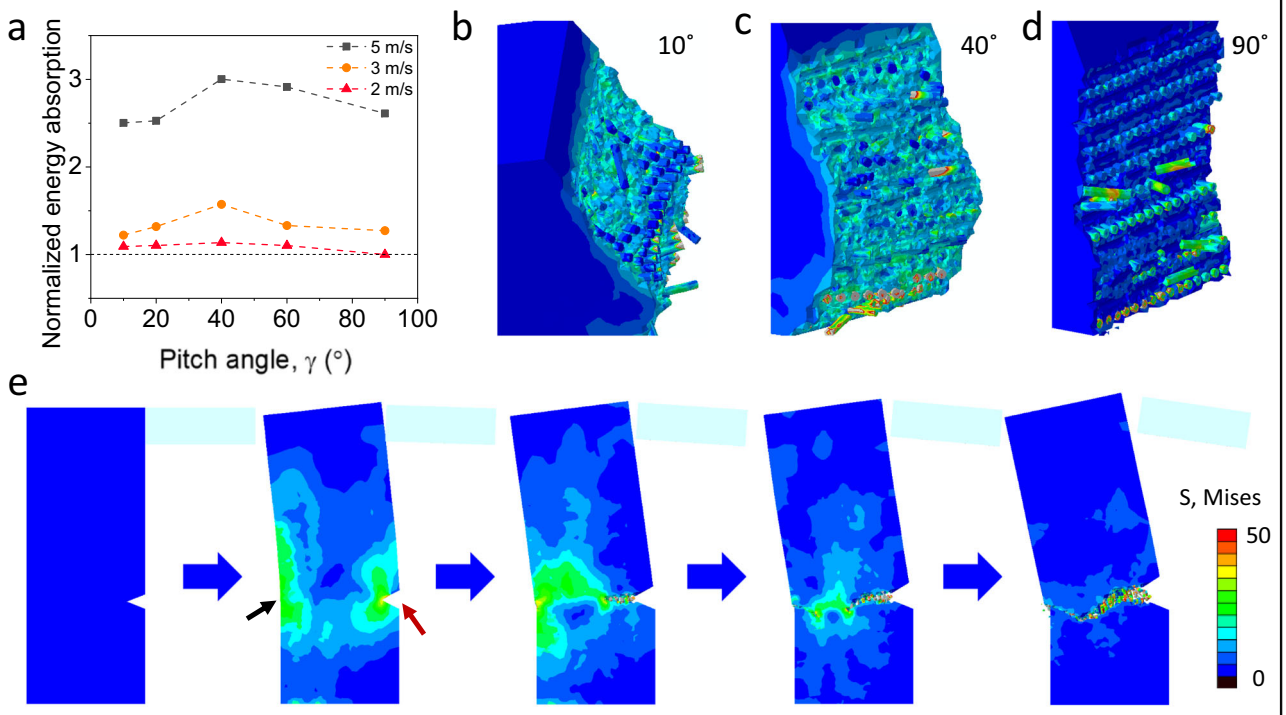

Fig. 5 Simulation of the fracture of the Bouligand composites under impact. a Energy absorption of the Bouligand composites normalized by the energy absorption levels of the composites at $\gamma = 90°$ as a function of the pitch angle under impact at different speeds (2 m/s, 3 m/s and 5 m/s). Fracture morphologies of the fractured Bouligand composites with γ values of (**b**) 10°, (**c**) 40°, and (**d**) 90°. **e** Snapshots showing the fracture of the Bouligand composite with $\gamma = 40°$ at an impact speed of 3 m/s from the top right corner (impactor represented by the light blue area). The color code represents the local tensile stresses. The black arrow near the clamp holder and red arrow at the notch tip indicate the stress concentration and crack initiation, respectively.

parameters, the resulting value of energy absorption could not be directly compared with the experimental results. Therefore, the value was substituted with the normalized energy absorption. The simulation of the impact tests of the Bouligand composites with pitch angles from 10° to 90° revealed a maximum energy absorption at 40°, confirming the experimental results (Fig. 5a and SI Table S3). With increasing impact speed, the maximum value was still obtained at a pitch angle of 40° for all speeds. This finding indicated that the impact speed did not affect the optimum pitch angle. Furthermore, the impact speed (strain rate) influenced the continuum damage of the epoxy matrix, thereby playing a role in the energy absorption of the composites; however, the value was lower than those of Bouligand composites, as shown in SI Table S3. Therefore, the increased energy absorption of the composites as the impact speed increased was attributed to the Bouligand structure. This phenomenon, wherein a high impact speed resulted in additional energy absorption during failure, was confirmed in laminated structures[27].

After impact failure, the fracture morphologies presented crack propagation features similar to those in the experiments. In Bouligand structures with γ of 10°, the crack propagated along the microfibers, revealing crack twisting as the dominant fracture mode (Fig. 5b). Upon increasing γ to 40°, crack twisting and crack bridging along the microfiber orientation were observed (Fig. 5c). In the Bouligand structure with γ of 90°, the crack twisted when the microfibers were parallel to the notch direction, while crack bridging occurred when the microfibers were perpendicular to the notch direction (Fig. 5d). Therefore, we could confirm the transition from crack twisting to crack bridging at an optimum pitch angle of 40°. In addition, the numerical simulations provided information on the mode by which the composite fractured during impact. Figure 5e and SI Video S2 illustrated the entire failure at an impact speed of 3 m/s for the Bouligand composite with $\gamma = 40°$. Before impact, the sample was relaxed, and no stress was observed at its surface. Once the pendulum struck, stresses quickly accumulated at the notch tip (red arrow) and in the opposite region near the clamp holder (black arrow). These stress concentrations led to cracking at these regions, which then propagated and eventually met each other. Moreover, when examining the Bouligand composites with $\gamma = 40°$ at a low impact speed of 2 m/s, there was a negligible difference in fracture behavior relative to the composites at an impact

speed of 3 m/s (see SI, Fig. S11a). This slight difference was indicative of a minor enhancement in energy absorption. However, with an increase in impact speed of 5 m/s, the Bouligand composites with $\gamma = 40°$ revealed additional crack tortuosity and fracture roughness, therefore resulting in further energy absorption (see SI, Fig. S11b and Table S3). With a further increase in the impact speed to 10 m/s, the composites were destroyed at the impact location, as marked by the red arrow, and it was difficult to estimate the energy absorption and the fracture mechanism (see SI, Fig. S11c). Therefore, the Bouligand composites under high impact speeds beyond 10 m/s from the simulation could not be compared with the composites at lower impact speeds (e.g., 2, 3, and 5 m/s).

Likewise, the use of a matrix with a high mechanical strength and an increased impact speed could increase the energy absorption values without changing the optimum pitch angle (see SI, Tables S2 and S3, and Fig. S12 for simulations with a high-strength matrix).

Quasistatic bending test

The simulated results indicated the limited effect of the impact speed on the optimum pitch angle. This point is important since in practical applications, the composites undergo various types of loadings. Furthermore, other scholars have tested the quasistatic fracture of Bouligand composites with other compositions. Therefore, we performed 3-point bending tests to estimate the flexural performance of our Bouligand composites at various pitch angles (Fig. 6a). All composites exhibited a flexural strength between 20 and 40 MPa and a flexural modulus between 1.6 and 2.4 GPa, which were relatively high strengths and moduli for 3D printed fiber-reinforced polymers (Fig. 6b)[28]. These values could be optimized by choosing a stronger resin or other constituents in the ink. Interestingly, the Bouligand composites with a pitch angle of 40° exhibited the highest flexural strength and modulus, with values of 37 MPa and 2.26 GPa, respectively. These values were 48% and 28% greater than those of the composites with pitch angles of 10° and 90°, respectively. In contrast, the Bouligand composites with a pitch angle of less than 40° exhibited a relatively high strain at fracture. For instance, the composites with a pitch angle of 10° broke at 4% strain, whereas composites with a pitch angle of 90° broke at 2% strain (Fig. 6c). The composites with small pitch angles showed crack twisting and a large fracture surface area, resulting in increased strain at failure, whereas composites with high pitch angles showed crack bridging and straight cracks, resulting in decreased flexural strain at failure. Furthermore, calculation of the flexural energy absorption E_s by integrating the force–displacement curves yielded an estimate of the quasistatic toughness of the composites. When plotting E_s as a function of the pitch angle, 40° was still the pitch angle yielding the highest value (Fig. 6d). E_s increased linearly from $\gamma = 10°$ to 40°, reaching a maximum value of 8 kJ/m^2 at $\gamma = 40°$. However, beyond a 40° pitch angle, E_s largely decreased to 4 kJ/m^2 at $\gamma = 90°$. Finally, the crack path in the Bouligand composites with $\gamma = 40°$ showed high tortuosity, which likely contributed mostly to the energy absorption during testing (Fig. 6e). Electron micrographs of the fractured surface displayed the combined fracture mechanisms with crack twisting and crack bridging (Fig. 6f). These results confirmed the limited influence of impact speed according to the simulations.

Discussion

In this work, we 3D print discontinuous glass microfiber composites with controlled microstructures using DIW. The composites with unidirectional orientation possess a maximum energy absorption of 1.1 kJ/m^2 at $\alpha = 90°$, where the microfibers are perpendicular to the impact direction. By building Bouligand composites with microfibers at $\alpha = 90°$, increased impact energy absorption is obtained at a pitch angle of $\gamma = 40°$ with values reaching 2.5 kJ/m^2, representing a 140% increase relative to the unidirectional composites. Moreover, a strong correlation between surface roughness and energy absorption in Bouligand composites is revealed. The surface roughness can be used to estimate the impact resistance performance of Bouligand composites in the future. From the fracture morphologies, we observe hybrid fracture mechanisms with crack twisting and crack bridging models in Bouligand composites during low-velocity impact in the experiment (3.5 m/s) and in the numerical simulation (2–5 m/s). As the pitch angle increases, the fracture surface morphologies transition from crack twisting-dominated patterns to crack bridging-dominated patterns. In addition to dynamic impact, the flexural strength and modulus values of the Bouligand composites at $\gamma = 40°$ exhibit maximum values of 37 MPa and 2.26 GPa, respectively.

Because of the use of DIW as the 3D printing process, we find that the absence of microvoids, the low porosity and the good interface binding between each deposited filament prevent macroscopic delamination under impact loading relative to the reported results in FDM composites[6]. Furthermore, previous scholars have reported that the increase in microfiber loading results in additional microfiber slippage and pull-out, enabling increased impact energy absorption[28]. In this work, microfiber concentrations exceeding 35 wt% in the ink can be prepared by adjusting the contents of carbon black and CNTs. Therefore, we can improve the impact performance using a high concentration of glass fibers in Bouligand composites according to the practical application. Furthermore, surface modification of glass microfibers

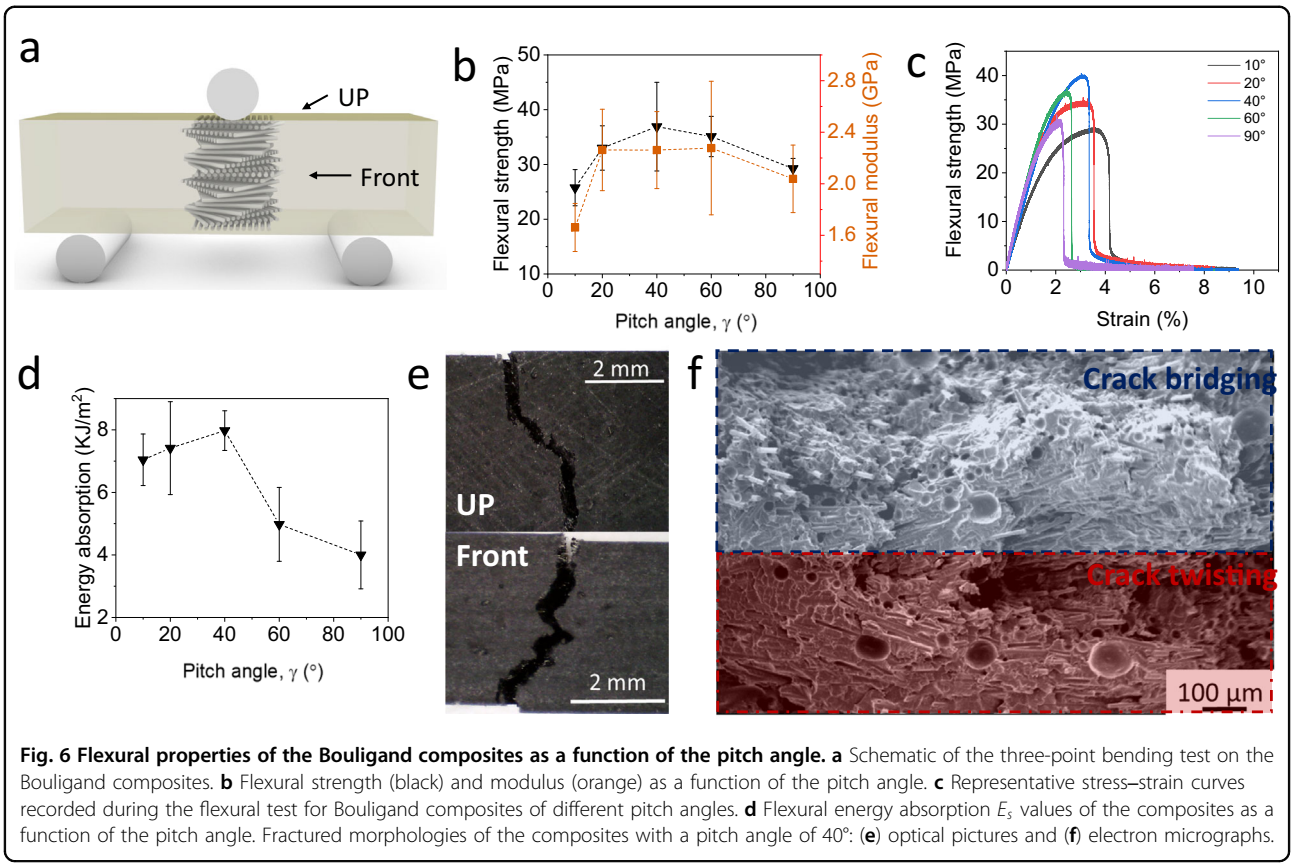

Fig. 6 Flexural properties of the Bouligand composites as a function of the pitch angle. a Schematic of the three-point bending test on the Bouligand composites. **b** Flexural strength (black) and modulus (orange) as a function of the pitch angle. **c** Representative stress–strain curves recorded during the flexural test for Bouligand composites of different pitch angles. **d** Flexural energy absorption E_s values of the composites as a function of the pitch angle. Fractured morphologies of the composites with a pitch angle of 40°: (**e**) optical pictures and (**f**) electron micrographs.

using small molecules, such as silane coupling agents, to improve the interface compatibility with the matrix is an option to enhance the performance of the Bouligand composites[29]. As reported by Kaijin et al.,[7] the longer aspect ratio of the fiber decreases the critical pitch angle and further enhances the energy absorption level. In our work, the aspect ratio of glass fibers is 2–30, which is shorter than the fibers in the beetle exoskeleton (aspect ratio of 50)[30]. To properly increase the aspect ratio of fibers and avoid clogging at the tip of the nozzle, thin commercial glass fibers and carbon fibers can be employed in the fabrication of Bouligand composites. Moreover, biomaterials, such as hydroxyapatite mineral microfibers and SiC whiskers, can be introduced in this ink to extend their applications. Although the fracture mechanism is observed at low-velocity impact in this work, determining the fracture performance values of the Bouligand composite under high-velocity or even hyper-velocity impact conditions is an interesting topic for future investigations.

In summary, this unique printing technique allows simultaneous microstructure and macroscopic shape design to enhance the mechanical properties, particularly the impact resistance, and to extend the practical applications of fiber composites in the aerospace, automotive, and defense industries, among others.

Acknowledgements
This research was funded by the National Research Foundation of Singapore, Singapore (Award NRFF12 2020–0002). We acknowledge Peifang Dee for helping with the micro-CT test.

Author details
[1]School of Mechanical and Aerospace Engineering, Nanyang Technological University, 50 Nanyang Avenue, Singapore 639798, Singapore. [2]School of Materials Science and Engineering, Nanyang Technological University of Singapore, 50 Nanyang Avenue, Singapore 639798, Singapore. [3]Singapore Centre for 3D printing, Nanyang Technological University of Singapore, 50 Nanyang Avenue, Singapore 639798, Singapore

Author contributions
G.L.: writing – original draft, visualization, investigation, data curation, and conceptualization. P.W.: writing—review and editing, data curation, and investigation. R.N.J.W.: writing—review and editing, data curation, and investigation. F.J.: writing—review and editing, investigation, and data curation. L.F.H.: writing—review and editing, conceptualization, supervision, and funding acquisition.

Data availability
All data are available in this manuscript and in the attached supplementary files. Additional information can be requested from the authors.

Conflict of interest
The authors declare no competing interests.

Supplementary information The online version contains supplementary material available at https://doi.org/10.1038/s41427-023-00508-6.

Received: 26 June 2023 Revised: 28 September 2023 Accepted: 4 October 2023
Published online: 24 November 2023

References

1. Le Ferrand, H., Bouville, F., Niebel, T. P. & Studart, A. R. Magnetically assisted slip casting of bioinspired heterogeneous composites. *Nat. Mater.* **14**, 1172–1179 (2015).
2. Patek, S. N. & Caldwell, R. L. Extreme impact and cavitation forces of a biological hammer: strike forces of the peacock mantis shrimp Odontodactylus scyllarus. *J. Exp. Biol.* **208**, 3655–3664 (2005).
3. Weaver, J. C. et al. The stomatopod dactyl club: a formidable damage-tolerant biological hammer. *Science* **336**, 1275–1280 (2012).
4. Guarín-Zapata, N., Gomez, J., Yaraghi, N., Kisailus, D. & Zavattieri, P. D. Shear wave filtering in naturally-occurring Bouligand structures. *Acta Biomater.* **23**, 11–20 (2015).
5. Liu, J., Li, S., Fox, K. & Tran, P. 3D concrete printing of bioinspired Bouligand structure: a study on impact resistance. *Addit. Manuf.* **50**, 102544 (2022).
6. Yin, S. et al. Tough nature-inspired helicoidal composites with printing-induced voids. *Cell Rep. Phys. Sci.* **1**, 100109 (2020).
7. Wu, K. et al. Discontinuous fibrous Bouligand architecture enabling formidable fracture resistance with crack orientation insensitivity. *Proc. Natl Acad. Sci. USA* **117**, 15465–15472 (2020).
8. Apichattrabrut, T. & Ravi-Chandar, K. Helicoidal composites. *Adv. Mater. Struct.* **13**, 61–76 (2006).
9. Cheng, L., Thomas, A., Glancey, J. L. & Karlsson, A. M. Mechanical behavior of bio-inspired laminated composites. *Compos. - A: Appl. Sci.* **42**, 211–220 (2011).
10. Grunenfelder, L. K. et al. Bio-inspired impact-resistant composites. *Acta Biomater.* **10**, 3997–4008 (2014).
11. Chen, S.-M. et al. Biomimetic twisted plywood structural materials. *Natl Sci. Rev.* **5**, 703–714 (2018).
12. Luo, Y. et al. Modulating of bouligand structure and chirality constructed bionically based on the self-assembly of chitin whiskers. *Biomacromolecules* **24**, 2942–2954 (2023).
13. Yang, Y. et al. Recent progress in biomimetic additive manufacturing technology: from materials to functional structures. *Adv. Mater.* **30**, 1706539 (2018).
14. Yang, Y. et al. Biomimetic anisotropic reinforcement architectures by electrically assisted nanocomposite 3D printing. *Adv. Mater.* **29**, 1605750 (2017).
15. Hausmann, M. K. et al. Dynamics of cellulose nanocrystal alignment during 3D printing. *ACS Nano* **12**, 6926–6937 (2018).
16. Saadi, M. A. S. R. et al. Direct ink writing: a 3D printing technology for diverse materials. *Adv. Mater.* **34**, 2108855 (2022).
17. Corker, A., Ng, H. C. H., Poole, R. J. & García-Tuñón, E. 3D printing with 2D colloids: designing rheology protocols to predict 'printability' of soft-materials. *Soft Matter* **15**, 1444–1456 (2019).
18. Cantwell, W. J. & Morton, J. The impact resistance of composite materials — a review. *Composites* **22**, 347–362 (1991).
19. Puthanveetil, S., Liu, W. C., Riley, K. S., Arrieta, A. F. & Le Ferrand, H. Programmable multistability for 3D printed reinforced multifunctional composites with reversible shape change. *Compos. Sci. Technol.* **217**, 109097 (2022).
20. Püspöki, Z., Storath, M., Sage, D. & Unser, M. in *Focus on Bio-Image Informatics* (eds. De Vos, W. H., Munck, S. & Timmermans, J.-P.) 69–93 (Springer International Publishing, Cham, 2016).
21. Sun, L., Gibson, R. F., Gordaninejad, F. & Suhr, J. Energy absorption capability of nanocomposites: a review. *Compos. Sci. Technol.* **69**, 2392–2409 (2009).
22. Guan, L.-Z. et al. Mechanical properties and fracture behaviors of epoxy composites with phase-separation formed liquid rubber and preformed powdered rubber nanoparticles: A comparative study. *Polym. Compos.* **36**, 785–799 (2015).
23. Ding, Y., Zeng, W., Wang, Q. & Zhang, Y. Topographical analysis of fractured surface roughness of macro fiber reinforced concrete and its correlation with flexural toughness. *Constr. Build Mater.* **235**, 117466 (2020).
24. Erdem, S. & Blankson, M. A. Fractal–fracture analysis and characterization of impact-fractured surfaces in different types of concrete using digital image analysis and 3D nanomap laser profilometery. *Constr. Build Mater.* **40**, 70–76 (2013).
25. Ficker, T. & Martišek, D. Digital fracture surfaces and their roughness analysis: applications to cement-based materials. *Cem. Concr. Res.* **42**, 827–833 (2012).
26. Yan, X., Reiner, J., Bacca, M., Altintas, Y. & Vaziri, R. A study of energy dissipating mechanisms in orthogonal cutting of UD-CFRP composites. *Compos. Struct.* **220**, 460–472 (2019).
27. Zhang, X., Wu, K., Ni, Y. & He, L. Anomalous inapplicability of nacre-like architectures as impact-resistant templates in a wide range of impact velocities. *Nat. Commun.* **13**, 7719 (2022).
28. H R, M. et al. Effect of short glass fiber addition on flexural and impact behavior of 3D printed polymer composites. *ACS Omega* **8**, 9212–9220 (2023).
29. Park, S.-J. & Jin, J.-S. Effect of silane coupling agent on interphase and performance of glass fibers/unsaturated polyester composites. *J. Colloid Interface Sci.* **242**, 174–179 (2001).
30. Yang, R., Zaheri, A., Gao, W., Hayashi, C. & Espinosa, H. D. AFM identification of beetle exocuticle: bouligand structure and nanofiber anisotropic elastic properties. *Adv. Funct. Mater.* **27**, 1603993 (2017).